ACS APPLIED MATERIALS & INTERFACES

Research Article

www.acsami.org

Bioinspired Nanofeatured Substrates: Suitable Environment for Bone Regeneration

H. Rammal,[†,‡,●] M. Dubus,[†,‡,●] L. Aubert,[†,§] F. Reffuveille,[†,§] D. Laurent-Maquin,[†,‡] C. Terryn,[⊥] P. Schaaf,[¶,□] H. Alem,[■] G. Francius,[○] F. Quilès,[○] S. C. Gangloff,[†,§] F. Boulmedais,[□] and H. Kerdjoudj*[,†,‡]

[†]EA 4691, Biomatériaux et Inflammation en Site Osseux (BIOS), SFR-CAP Santé (FED 4231), Université de Reims Champagne Ardenne, 51100 Reims, France

[‡]UFR d'Odontologie, Université de Reims Champagne Ardenne, 51100 Reims, France

[§]UFR de Pharmacie, Université de Reims Champagne Ardenne, 51100 Reims, France

[⊥]Plateforme d'Imagerie Cellulaire et Tissulaire (PICT), Université de Reims Champagne Ardenne, 51100 Reims, France

[¶]INSERM, UMR-S 1121, "Biomatériaux et Bioingénierie", Fédération de médecine translationnelle de Strasbourg, Faculté de Chirurgie Dentaire, Université de Strasbourg, 67000 Strasbourg, France

[□]CNRS, Institut Charles Sadron UPR 22, Université de Strasbourg, 23 rue du Loess, 67034 Strasbourg Cedex, France

[■]CNRS, UMR 7198, Institut Jean Lamour (IJL), Université de Lorraine, 54500 Vandoeuvre Lès Nancy, France

[○]CNRS, UMR 7564, Laboratoire de Chimie Physique et Microbiologie pour l'Environnement (LCPME), Université de Lorraine, 54500 Vandoeuvre Lès Nancy, France

Supporting Information

ABSTRACT: Bone mimicking coatings provide a complex microenvironment in which material, through its inherent properties (such as nanostructure and composition), affects the commitment of stem cells into bone lineage and the production of bone tissue regulating factors required for bone healing and regeneration. Herein, a bioactive mineral/biopolymer composite made of calcium phosphate/chitosan and hyaluronic acid (CaP-CHI-HA) was elaborated using a versatile simultaneous spray coating of interacting species. The resulting CaP-CHI-HA coating was mainly constituted of bioactive, carbonated and crystalline hydroxyapatite with 277 ± 98 nm of roughness, 1 μm of thickness, and 2.3 ± 1 GPa of stiffness. After five days of culture, CaP-CHI-HA suggested a synergistic effect of intrinsic biophysical features and biopolymers on stem cell mechanobiology and nuclear organization, leading to the expression of an early osteoblast-like phenotype and the production of bone tissue regulating factors such as osteoprotegerin and vascular endothelial growth factor. More interestingly, amalgamation with biopolymers conferred to the mineral a bacterial antiadhesive property. These significant data shed light on the potential regenerative application of CaP-CHI-HA bioinspired coating in providing a suitable environment for stem cell bone regeneration and an ideal strategy to prevent implant-associated infections.

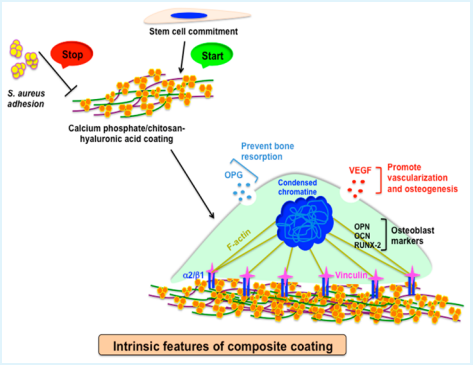

KEYWORDS: *bone regeneration, bioinspired coating, human stem cells, mechanobiology, stem cell differentiation, nanomedicine*

INTRODUCTION

Upon placement of bone material into a host environment, a sequence of complex and strongly interrelated cell and matrix events takes place, leading to bone healing. Such processes are strongly controlled by the surface properties of the prosthesis in terms of roughness, elasticity, porosity, and chemical composition.[1] Apatite-like calcium phosphate, successfully used in orthopedic and dental fields, is a biomimetic material with good biocompatibility, bioactivity, and osteoconductivity, but it lacks osteoinductivity. For ideal bone material, osteoinductivity, an ability to induce the differentiation of stem cells into osteogenic lineage, is required in combination with osteoconductivity. Because bone is composed of organic as well as inorganic material, organic/inorganic composites are considered as a promising approach toward functional bone implant coatings.

Hyaluronic acid (HA) is a naturally occurring glycosaminoglycan present in vertebrate tissues and body fluid and is known to interact with cell surface receptors including CD44. The latter triggers intracellular signals that influence cellular

Received: February 3, 2017
Accepted: March 16, 2017
Published: March 16, 2017

DOI: 10.1021/acsami.7b01665
ACS Appl. Mater. Interfaces 2017, 9, 12791−12801

adhesion, proliferation, differentiation, migration, and survival.[2] Among natural polymers, chitosan (CHI), obtained by deacetylation of chitin, is a biocompatible polysaccharide with a weak cationic charge that is largely exploited in biomedical applications.[3] CHI is likely to form complexes with polyanionic HA which are thus commonly used for drug encapsulation,[4] gene delivery nanoparticles,[5] implant coatings,[4] as well as scaffolds for cartilage[6] and bone regenerative medicine, promoting osteoblast maturation and impairing bacterial activity.[7]

Organic/inorganic composite coatings are expected to display properties for osteointegration superior to those of their single constituents.[8] However, the fabrication of composite coatings with controlled architectures seems challenging. Generally, inorganic calcium phosphate (CaP) deposition techniques are characterized by extreme processing conditions in terms of temperature and pressure, contrary to organic biomolecules, where coatings need to be applied under physiological conditions because biomolecules do not tolerate high temperatures or other extreme conditions. Moreover, deposition techniques are line-of-sight processes, which complicate coatings of complex-shaped substrates and further up-scaling to large-scale production.

A new and straightforward method based on simultaneous spray coating of interacting species (SSCIS) process was used to design an inorganic substrate.[9] Harmful solvents and harsh processing conditions are not required, making SSCIS an attractive technique for biological-based applications. This friendly automated system is a low temperature process applicable to any heat sensitive substrate, including natural polymers. It possesses the additional advantage that spray technology can easily be adapted in industrial production. We recently demonstrated that spraying saturated calcium and phosphate solutions (50 spray cycles) led to the formation of bioactive calcium phosphate substrates with controlled nanoroughness, inducing the formation of bone-like nodule after 4 weeks of stem cell culture without any osteogenic supplements.[10] Inclusion of biopolymers such as CHI and HA to CaP using the SSCIS process is thought to provide a suitable environment for bone regeneration along with prevention of implant infections. In the following, detailed physicochemical, mechanical, and bioactive insights into calcium phosphate supplemented with chitosan and hyaluronic acid polymers (CaP-CHI-HA) were provided before testing its intrinsic biological features. At one week of culture and in the absence of osteogenic supplements, CaP-CHI-HA impacted adhesion and morphology of stem cells, leading to the early osteoblastic differentiation and secretion of factors regulating bone resorption and vascularization. Moreover, CaP-CHI-HA was able to reduce significantly *Staphylococcus aureus* adhesion, a common pathogen in orthopedic surgery.

RESULTS AND DISCUSSION

Composites designed to interact with cells by emulating features of the bone extracellular matrix comprise calcium phosphates and natural biopolymers. Here, by using simultaneous spray coating of interacting species process, we elaborated calcium phosphate composite coating CaP-CHI-HA. CaP coating, obtained in the same conditions as published elsewhere (i.e. 50 simultaneous spray cycles for 2 s),[10] was used as control. Macroscopic views of CaP-CHI-HA and CaP substrates showed a whitish deposition on the top of the coverslip glass (Figure 1A). Scanning electron microscopy

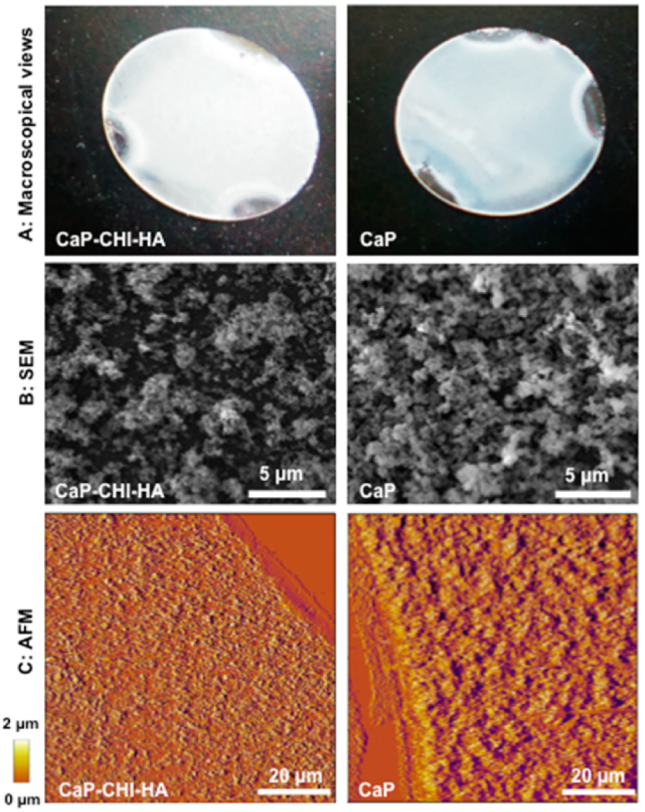

Figure 1. Surface features of CaP-CHI-HA compared to CaP. (A) Macroscopic images. (B) Top views of representative SEM images (scale bars indicate 5 μm). (C) Representative AFM map (scale bars indicate 20 μm) obtained in contact mode in dry conditions.

(SEM) images confirmed the effective deposition of both coatings displaying similar spherical aggregates without any pores or cracks on the surface (Figure 1B). In general, we found slight changes in the dimensions of the aggregates, which seemed smaller once biopolymers were included, resulting in smoother and thinner coatings. Atomic force microscopy (AFM) imaging highlighted a roughness of 277 ± 98 nm for CaP-CHI-HA nanostructured surfaces in comparison to 374 ± 191 nm for CaP with a thickness of around 1 μm (Table 1 and

Table 1. CaP-CHI-HA and CaP Features Obtained by Atomic Force Microscopy in Contact Mode and Aqueous Medium Condition (DMEM)

	CaP-CHI-HA	CaP
thickness (μm)	1.24 ± 0.5	1.3 ± 0.5
roughness (nm)	277 ± 98	374 ± 191
elastic modulus (kPa)	2280 ± 1071	6457 ± 1987

Figure 1C). The amalgamation with biopolymers is expected to confer toughness and flexibility to strong and hard minerals.[11] Elastic moduli of both coatings, measured by AFM nanoindentation, indicated a softer CaP-CHI-HA (2.3 ± 1.1 GPa) compared to CaP (6.4 ± 1.9 GPa). Thus, elastic modulus of CaP-CHI-HA is in reasonable agreement with the value of 2 GPa reported for trabecular bone.[12]

Development of bone-like coatings often requires low thickness (less than 10 μm) and bone-like tensile properties.[13] On the basis of our findings, physical features of the resulting CaP-CHI-HA coating meet the above cited criteria guidelines

DOI: 10.1021/acsami.7b01665
ACS Appl. Mater. Interfaces 2017, 9, 12791−12801

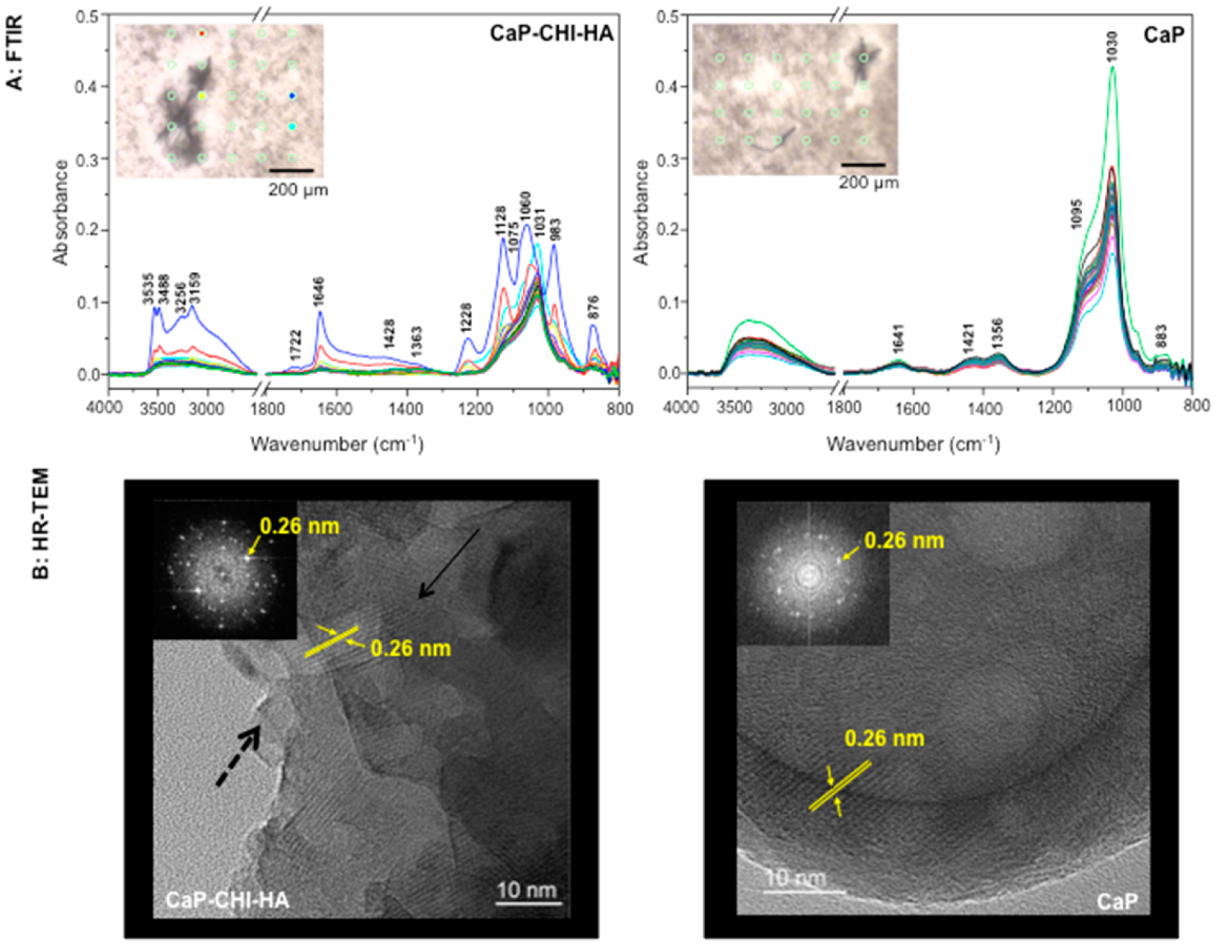

Figure 2. Chemical composition of CaP-CHI-HA compared to CaP. (A) Spectra obtained by Fourier transform infrared microspectroscopy in transmission mode. Inserts: optical images with the measurement points (scale bars indicate 200 μm). Colored points indicating dicalcium phosphate dehydrate. (B) HR-TEM images of the crystal-like structure (inserts: electron diffraction, scale bars indicate 10 nm). Arrows and dashed arrows indicate mineral crystal and amorphous film, respectively.

and thus could be suitable to be used in the field of orthopedic and dental implants.

Confocal Raman and infrared microspectroscopies were conducted to identify the functional groups of both coatings. Data for main vibration bands are compiled in Tables S1 and S2. Raman spectra recorded on 0.01 mm^2 indicated that the main vibration bands of CaP-CHI-HA were attributed to nonstoichiometric hydroxyapatite (see Figure S1A and Table S1 in the Supporting Information for details) and is consistent with CaP published data.[10] The well-preserved characteristic peaks of hydroxyapatite in the spectra of CaP-CHI-HA suggested no significant structural change or transformation of hydroxyapatite throughout inclusion of biopolymers. Micro-infrared spectra recorded on 0.24 and 0.29 mm^2 areas showed slight differences between CaP-CHI-HA and CaP in terms of crystallinity, homogeneity, hydration, and amount of deposit mineral (chemical maps provided in Figure S1B), which could be attributed to differences in topography of coatings.[14] Main vibration bands of CaP-CHI-HA showed a carbonated poorly crystalline hydroxyapatite and in some places a dicalcium phosphate dihydrate phase,[15] whereas CaP revealed only a carbonated poorly crystalline hydroxyapatite[16] (Figure 2A and Table S2). CHI and HA bands were not detected because of the very weak intensity bands and a strong overlapping with those of hydroxyapatite and water.[17] High resolution-transmission electron microscopy (HR-TEM) combined with electron diffraction, the benchmark "gold standard" technique for the determination of crystal structure for any given mineral, was also performed (Figures 2B and S1C). Our results revealed that the CaP-CHI-HA substrate displayed crystalline particles dispersed on an amorphous organic film derived from self-assembly of polymers that hampered the determination of particle size. Related to CaP, crystalline particles with elliptical shaped spheres displayed a large axis of about 92 ± 10 nm and a small axis of 80 ± 7 nm. Dark parts were due to the assembly of several crystals on the top of each other, leading to the increase in thickness. Electron diffraction showed concentric spotty rings, revealing the crystalline nature of the hydroxyapatite (see inserts in Figure 2B), as confirmed by the calculated 0.26 nm *d*-spacing from the fast Fourier transform (Table S3). The degree of crystallinity, determined by X-ray diffraction, was 29% for CaP-CHI-HA and 34% for CaP (data not shown), in accordance with the infrared data that showed spectra of poor crystalline hydroxyapatite.

The bioactivity of calcium phosphates has been attributed to different factors such as their ability to modulate calcium and phosphate ions in solution, which could be influenced by their degree of crystallinity.[18,19] The fluctuation of ions in physiological solution can be indicative of ion dissolution from the calcium phosphate or ion precipitation from solution,

DOI: 10.1021/acsami.7b01665
ACS Appl. Mater. Interfaces 2017, 9, 12791−12801

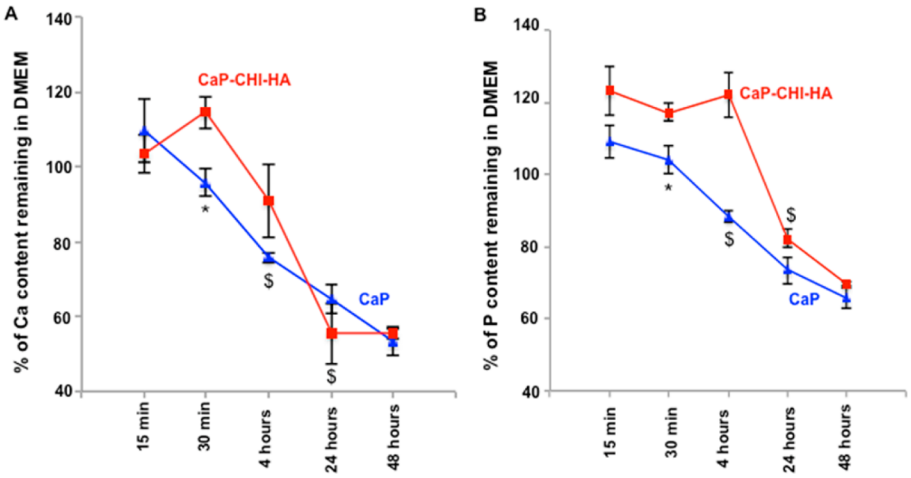

Figure 3. Bioactivity of CaP-CHI-HA compared to CaP. Graphs of percentage content of calcium (A) and phosphorus (B) ions remained in culture medium analyzed by ICP-OES, showing two distinct phenomena: (i) nonsignificant increase in Ca and P content (red and blue lines) at 15 min, reflecting a relative stability of both coatings, and (ii) significant decrease in Ca and P content (red line at 24 h and blue line at 4 h), indicating a delay of ion precipitation from DMEM in the presence of CHI and HA (*CaP versus CaP-CHI-HA and $ CaP or CaP-CHI-HA versus previous time, $n = 3$, t-test).

leading to the formation of a bioactive layer. Thus, the percentage of Ca and P content remaining in solution after substrate incubation in DMEM culture medium was monitored (Figures 3A and B). After 15 min of soaking in DMEM, a slight increase in calcium ions was observed for both coatings. In contrast, CaP-CHI-HA was found to release more phosphorus ions compared to CaP. The nonsignificant increase in both ions in DMEM means that both coatings are relatively stable. Calcium and phosphorus precipitation from DMEM onto sprayed surfaces may promote the formation of a new bioactive layer.[10,18] We noticed that ion precipitation from DMEM onto CaP-CHI-HA was delayed compared to that onto CaP (24 h versus 4 h), which could be attributed to the differences in crystallinity and roughness of the coatings.[18] The presence of chitosan and hyaluronic acid is thought to act as a shield, delaying the formation of the bioactive layer. Moreover, the affinity of glycosaminoglycan as hyaluronic acid with calcium ions might also influence bioactivity kinetics.[4,20−22] Hence, the effect of organic molecules on the kinetic release and precipitation of ions from the substrate was clearly observed.

Stem cells are a heterogeneous population which exert their therapeutic effect by differentiating into osteoblasts and by secreting soluble factors promoting (i) activation of tissue-associated progenitors (bone morphogenic protein, BMP-2) and angiogenesis (vascular endothelial growth factor, VEGF) and (ii) inhibiting osteoclastogenesis (osteoprotegerin, OPG).[23,24] In the following, we investigated the response of stem cells derived from Wharton's jelly (WJ-SCs) to CaP-CHI-HA sprayed coating in view of their potential commitment into osteogenic lineage and their ability to release paracrine factors (i.e., VEGF, BMP-2, and OPG). CaP and coverslips were used as controls. In the case of osteoblast commitment, the effect of biophysical signal is associated with changes in cell morphology from fibroblastic (i.e., characterizing stem cells) to polygonal shape (i.e. characterizing osteoblasts).[25] After five days of culture, WJ-SCs on both coatings showed striking changes in cell morphology along with polygonal shape compared to the fibroblastic shape observed on coverslips (Figures 4A1−C1). A cascade of events is established during osteoblast differentiation, including expression of $\alpha 2/\beta 1$ integrin at the membrane, recruitment of vinculin at the focal adhesion complexes with the reorganization of cytoskeleton, nuclear changes, and expression of bone specific markers such as Runx-2, osteopontin (OPN), and osteocalcin (OCN),[26] and are thus described in the following.

Labeling $\alpha 2$ and $\beta 1$ integrin subunits revealed a strong expression at the membrane of WJ-SCs grown on CaP-CHI-HA and on CaP compared to that of cells maintained on the coverslip (Figures 4A2 and 3, B2 and 3, and C2 and 3). Confocal snapshots showed that for all conditions both cytoplasmic and focal adhesion complex vinculin were stained (Figures 4A4−C4). However, on both coatings, vinculin was more prominent and abundantly concentrated at the extreme edges of the cell, whereas on the coverslip, vinculin was evenly distributed throughout the cell body.

Vinculin, linked to focal adhesion mechanosensors, is a key molecule that links the actin cytoskeleton and integrins at the membrane. Its recruitment and stabilization to the focal adhesions complex is reinforced by internal cytoskeleton induced tension and reorganization.[27] This latter was further checked by labeling cell cytoskeleton (F-actin fibers) (Figures 4A5−C5). While WJ-SCs grown on both coatings exhibited perpendicularly oriented F-actin fibers gathering around the nuclei, WJ-SCs grown on the coverslip showed F-actin fibers parallel to the longitudinal cell axis and embedded nuclei within cytoskeleton network (Figure S2). Mechanical forces activate crosstalk between cytoskeleton and focal adhesion signaling, enabling the cell to sense and respond to the external stimuli.[28] Consistent with these previous findings, our results agreed with the hypothesis that spatial organization of F-actin is a determinant factor for cell stiffness. Indeed, AFM nano-indentation experiments showed that WJ-SCs grown for 5 days on both coatings exhibited a stiffer cytoplasm (24.8 ± 9.5 and 18.5 ± 8.2 kPa for CaP-CHI-HA and CaP, respectively) compared to that exhibited on the coverslip (8.7 ± 2.5 kPa) (Figure 4D). Extracellular-derived HA plays a regulatory role in controlling cell physiology through its interaction with CD44 receptor, inducing F-actin organization.[5,29] WJ-SCs express at membrane multipotent markers as CD44.[30] Taken together, our results suggest a potential synergistic effect of surface

DOI: 10.1021/acsami.7b01665
ACS Appl. Mater. Interfaces 2017, 9, 12791−12801

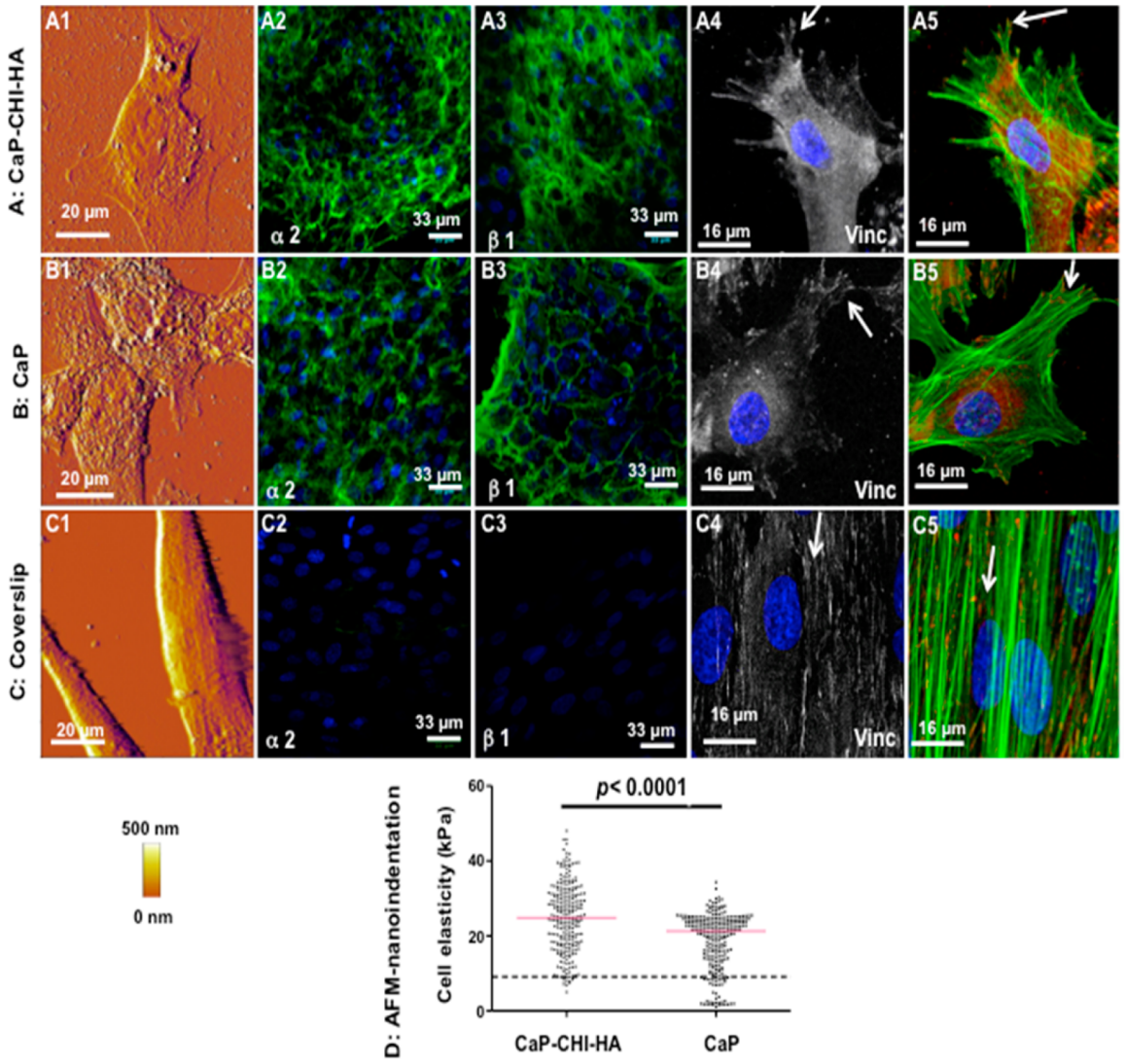

Figure 4. Wharton's jelly stem cell behavior. WJ-SCs cultured on CaP-CHI-HA (A), CaP (B), and coverslip (C) for five days were analyzed by AFM (A1, B1 and C1) and confocal fluorescent microscopy (A2−5, B2−5, and C2−5). AFM deflexion images showing polygonal-shaped cells on CaP-CHI-HA (A1) and CaP (B1) and fibroblastic-shaped cells on the coverslip (C1) (scale bars indicate 20 μm). Confocal fluorescent images of α2 and β1 integrins (green color) on CaP-CHI-HA (A2 and A3) and CaP (B2 and B3), showing cell−cell and cell−ECM contact distribution and lack of signal on coverslip (C2 and C3) (scale bars indicate 33 μm). Confocal images of vinculin (gray color), highlighting the vinculin distribution in both cytoplasm and focal adhesion complex on CaP-CHI-HA (A4) and CaP (B4) but only in the cytoplasm on the coverslip (C4). Confocal fluorescent images of F-actin cytoskeleton (green color) and vinculin (red color), confirming the formation of focal adhesion complex on CaP-CHI-HA (A5) and CaP (B5) in contrast to that on the coverslip (C5). White arrows indicate focal adhesion complex (scale bars indicate 16 μm). Graph of cell elasticity (D) corresponding to the 2D map in panels A1, B1, and C1, showing stiffer WJ-SCs on CaP-CHI-HA compared to those on CaP. Dashed bar corresponds to stiffness of WJ-SCs on the coverslip, and red bars indicate median (n = 50, Mann & Whitney test).

topography and HA/CD44 interaction on WJ-SC behavior. Changes in the cytoskeletal architecture may induce modifications of the nucleus shape, implying also variations of nuclear membrane permeability to factors involved in mechanotransduction.[31] Nuclei of stem cells are described to be more plastic than those of fully differentiated cells.[32] In addition to the evolution of nucleus shape (highlighted in Figure S2), nuclear volume and elongation were thus compared in all conditions. Marked increase in nucleus volume of cells grown on both coatings was obtained with 1878 ± 460 μm^3 for CaP-CHI-HA and 1455 ± 335 μm^3 for CaP compared to 811 ± 161 μm^3 for the coverslip (Figure 5A). Measurements of the long to short axis ratio revealed spherical nuclei shape (ratio ≤1.5) and elongated nuclei shape (ratio ≥1.8) for WJ-SCs grown on both coatings and the coverslip, respectively (Figure 5B).

DNA in the nucleus is grouped into chromosomes, each containing a linear DNA molecule associated with proteins that fold and pack the DNA into a more compact structure called chromatin. Chromatin condensation often correlates with the level of stem cell differentiation with less condensed chromatin organization in stem cell nuclei compared to localized hypercondensed regions in differentiated cell nuclei.[33] To determine if the observed changes in nucleus deformability influence chromatin condensation, we measured condensation of chromatin parameter (CCP) using the Sobel edge detection algorithm[34] (Figure 5C). On the basis of quantitative single cell imaging, the increase in CCP of WJ-SCs was correlated with an increase in nucleus volume with compacted and condensed

DOI: 10.1021/acsami.7b01665
ACS Appl. Mater. Interfaces 2017, 9, 12791−12801

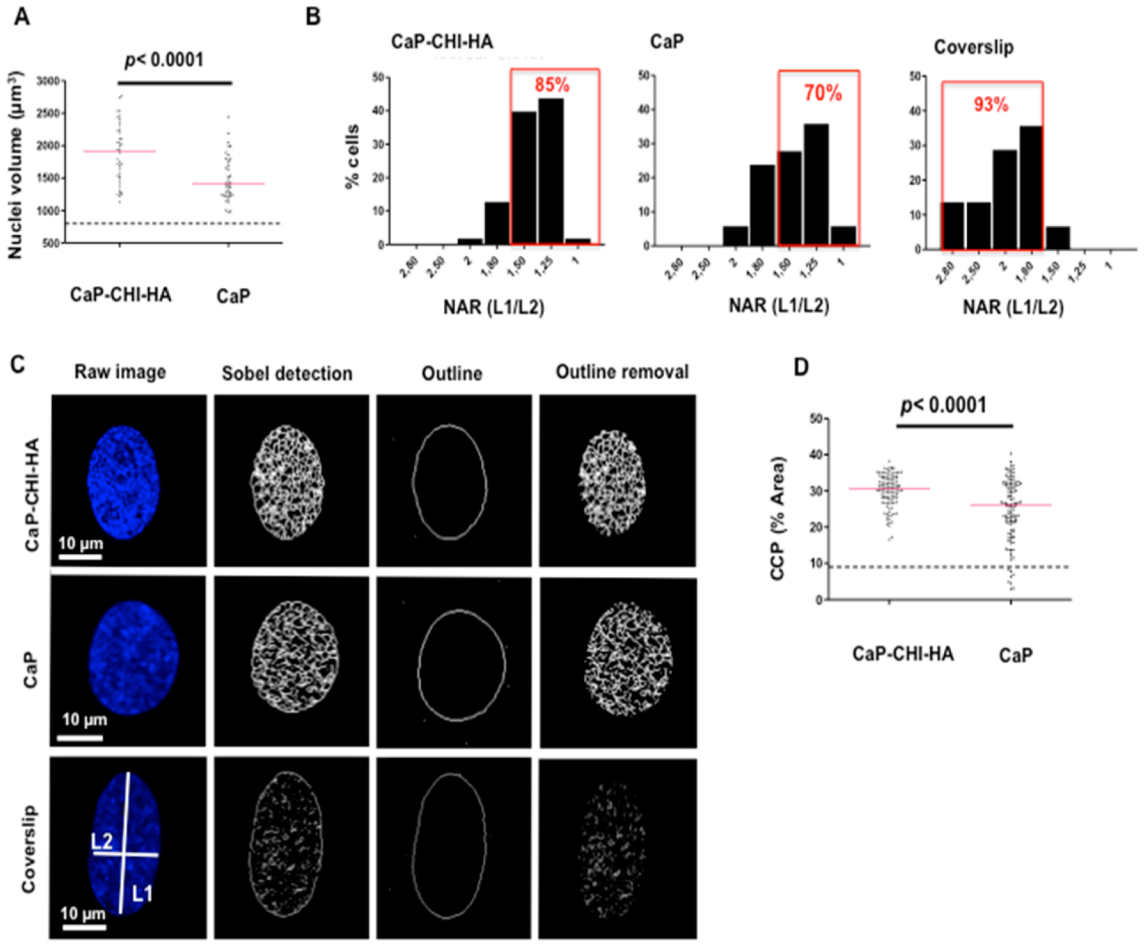

Figure 5. Nuclei features. (A) Nuclear volume of WJ-SCs determined by Imaris software, indicating volume of nuclei on CaP-CHI-HA > CaP > coverslip. (B) Nuclear aspect ratio (NAR) indicating rounded nuclei on CaP-CHI-HA (85% of total cells), CaP (70% of total cells) and elongated nuclei on the coverslip (93% of total cells). (C and D) Chromatin condensation parameter (CCP) determined by ImageJ software indicating CCP on CaP-CHI-HA > CaP > coverslip. L1 and L2 indicate long and short axis, respectively. Dashed bar (graphs) corresponds to nuclear volume of WJ-SCs on the coverslip, and red bars indicate median (scale bars = 10 μm, n = 50 cells, Mann & Whitney test).

chromatin in distinct foci for WJ-SCs grown on both coatings and a diffuse chromatin signal not restricted to distinct foci for cells grown on the coverslip (Figure 5C). During stem cell differentiation, some parts of DNA are silenced.[35] This silencing process involves global reorganization of chromatin,[36] including its condensation into distinct foci as described above. CCP of WJ-SCs grown on CaP-CHI-HA was significantly higher than CCP of WJ-SCs grown on CaP (Figure 5D), suggesting an early stem cell commitment on CaP-CHI-HA.

To confirm this commitment, the expression of bone-related proteins, including Runx-2, OPN, and OCN (i.e., described as early, intermediate, and late stage markers of osteoblast, respectively[5]), were followed by immunostaining after five days of culture (Figure 6A). A noteworthy difference in the expression and localization of these proteins was observed. WJ-SCs on both coatings showed a similar recognizable nuclear Runx-2 staining, whereas OPN and OCN had different localizations with a prominent cytoplasmic staining in cells grown on CaP-CHI-HA and a nuclear staining in cells on CaP. WJ-SCs cultured on the coverslip did not elicit any positive staining (Figure S3), signature of their undifferentiated state. Thus, immunofluorescence results seem to confirm that CaP-CHI-HA and CaP have the potential as a differentiation tool for directing WJ-SCs into an osteoblast-like phenotype in the absence of osteoinductive media. Furthermore, localization of bone-related proteins in WJ-SCs on CaP-CHI-HA, as described for mature osteoblasts, suggests an accelerating effect of CaP-CHI-HA on the early stem cell differentiation into an osteoblast-like phenotype.

Stem cells are also known to release local factors that create a more suitable osteogenic environment, including OPG, VEGF, and BMP-2.[37] OPG is known to disrupt bone-resorbing cells (activated osteoclasts), which have the ability to dissolve crystalline hydroxyapatite and degrade organic bone matrix.[38] VEGF is described as an attracting factor for endothelial cells as well as osteoblasts.[39] BMP-2 is described as a potent osteogenic factor able to commit stem cells into osteoblast lineage.[40] After a week of culture, ELISA protein quantification revealed a secretion of OPG and VEGF, whereas surprisingly BMP-2 was not detected in culture supernatants. WJ-SCs cultured on both coatings showed a modest increase in OPG secretion compared to those cultured on the coverslip (Figure 6B) and a significant increase in VEGF for WJ-SCs cultured on both coatings compared to those cultured on the coverslip (Figure 6C). Thus, WJ-SCs cultured on CaP-CHI-HA and CaP coatings are thought to provide a local environment that (i) blocks bone resorption through the inhibition of osteoclast activity and (ii)

DOI: 10.1021/acsami.7b01665
ACS Appl. Mater. Interfaces 2017, 9, 12791−12801

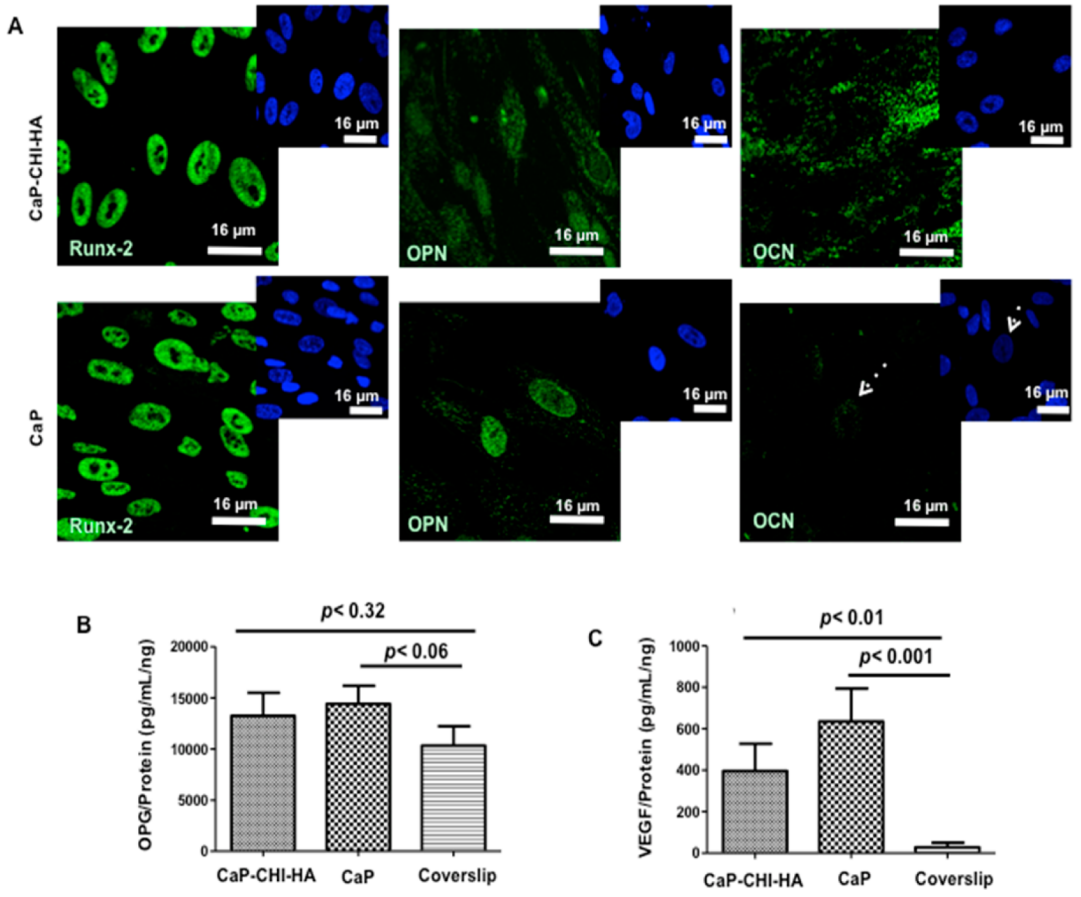

Figure 6. Wharton's jelly stem cell commitment and paracrine activities. (A) Confocal fluorescent images of Runx-2, OPN, and OCN expressed by WJ-SCs cultured on CaP-CHI-HA (upper line) and CaP (lower line). Inserts correspond to DAPI labeling nuclei (scale bars = 16 μm). Dashed arrow indicates nuclear localization of OCN on CaP. Production of OPG (B) and VEGF (C) quantified by ELISA, indicating a significant release by cells cultured on CaP-CHI-HA and CaP compared to that on the coverslip (results expressed by mean ± SEM, n = 6, Mann & Whitney test).

favors bone formation and vascularization through recruitment of host osteoblasts and endothelial cells, respectively.

While the above-cited results indicated the effectiveness of CaP-CHI-HA for bone regeneration, it is also of interest to investigate how such coating can affect the bacterial adhesion. Implant-associated infections are one of the most serious complications in orthopedic surgery. Common pathogens such as *S. aureus*, currently acquired at the time of surgery, attach to the surface of implants and potentiate the formation of complex biofilms, reducing the activity of antimicrobial agents.[41] An ideal strategy to combat implant-associated infections would be prevention of bacterial infection at the site of the implant. Chitosan possesses an intrinsic bactericidal activity through the interaction of its cationic amino groups with the negatively charged bacterial wall, suppressing biosynthesis, disturbing the mass transport across the bacterial wall, and accelerating the death process.[11] Although the bactericidal activity of chitosan was not demonstrated, our results showed a clear inherent antiadhesive effect of CaP-CHI-HA compared to that of CaP. In presence of both coatings at 37 °C for 48 h, adherent *S. aureus* on CaP-CHI-HA were 5 times less than that on CaP (Figure 7).

Reduction of bacterial adhesion on chitosan/hyaluronic acid multilayer film is attributed to a high number of carboxyl groups and ammonium groups.[42,43] Although Raman and infrared microspectroscopies did not reveal the presence of

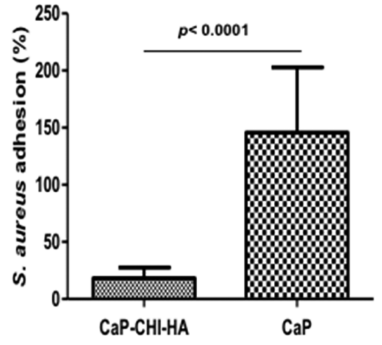

Figure 7. *S. aureus* adhesion. Graphs of the percentage of adhered bacteria to CaP-CHI-HA and CaP, showing a significant reduction of bacterial adhesion on CaP-CHI-HA compared to that on CaP (results expressed by mean ± SEM, n = 6, Mann & Whitney test).

biopolymers, the inherent antiadhesive property of CHI/HA was preserved in our coating.

CONCLUSION

Here, we reported a rationally bioinspired bone coating with intrinsic biophysical and chemical cues that provides a suitable environment for bone regeneration. Indeed, combining calcium phosphate to chitosan and hyaluronic acid biopolymers boosted the early stem cell differentiation into osteoblast-like lineage, maintained stem cell paracrine production of osteoprotegerin,

DOI: 10.1021/acsami.7b01665
ACS Appl. Mater. Interfaces 2017, 9, 12791−12801

and induced paracrine secretion of vascular endothelial growth factor. Moreover, amalgamation of biopolymers with minerals provided interesting functionalities, limiting *S. aureus* adhesion and thus providing an ideal strategy to combat implant-associated infections.

MATERIALS AND METHODS

1. Materials. Calcium nitrate ($Ca(NO_3)_2,4H_2O$), diammonium hydrogen phosphate ($(NH_4)_2HPO_4$), sodium dihydrogen phosphate hydrate (NaH_2PO_4), Tris(hydroxymethyl) aminomethane (Tris), calcium chloride hydrate ($CaCl_2$, $2H_20$), sodium chloride, and CHI (low molecular weight) from Sigma and HA (200 kDa) from Lifecore Biomedical were used without further purification. The salt solutions were prepared in ultrapure water (Millipore). For calcium phosphate composite substrate (CaP-CHI-HA), $CaCl_2$, $2H_20$ (0.32 M), and CHI 0.3 mg/mL were dissolved in NaCl (0.15 M)/HCl (2 mM) buffer (pH 4), whereas NaH_2PO_4 (0.19 M) and HA 0.3 mg/mL were prepared in NaCl (0.15 M) buffer (pH 10). For calcium phosphate (CaP) substrate, a calcium solution of $Ca(NO_3)_2{\cdot}4H_2O$ (0.32 M) and a phosphate solution of $(NH_4)_2HPO_4$ (0.2 M) were prepared in Tris buffer (10 mM Tris, pH 4 and 10, respectively). Coverslips of 14 mm diameter were provided from Thermo Scientific. Each experiment was preceded by a cleaning step of the coverslips with sodium dodecyl sulfate (100 mM, Sigma) for 15 min at 100 °C. After an intensive ultrapure water (Millipore) rinse, coverslips were brought in contact with HCl (100 mM, Sigma) for 15 min at 100 °C and finally rinsed with ultrapure water and kept at 4 °C.

2. Substrate Buildup. An automated spraying device was used for CaP-CHI-HA and CaP build-up. This device is constituted of four identical Airbrushes VL (Paasche, USA) nozzles. Each nozzle is pressurized by in-house compressed air line under a pressure of 1 bar and connected to solenoid valves. The spraying of the different solutions, following a chosen deposition sequence, is obtained by a succession of closings and openings of the valves controlled by homemade software. Three nozzles allow spraying of the calcium, the phosphate and of the rinsing solutions. The fourth nozzle, free of solution, is used for the drying step. The cleaned coverslip is mounted vertically on a mobile holder. For homogeneous buildup of CaP-CHI-HA and CaP coatings, the holder was rotated at 150 rpm. For the buildup of the coatings, both calcium and phosphate corresponding solutions were sprayed simultaneously on the coverslip for 2 s followed by a rinsing step of 2 s with ultrapure water and a drying step of 2 s under compressed air. These steps were repeated 50 times, and polymer concentrations were adjusted after calculation of flows during spraying to keep a charge ratio HA/CHI constant and equal to 0.7 to optimize the complex formation.[44]

3. Bioactivity Experiments. CaP-CHI-HA and CaP coatings were soaked in 1 mL of Dulbecco's modified Eagle's medium (DMEM, Gibco) at 37 °C. After 15 min, 30 min, 4 h, 24 h, and 48 h of incubation, the coatings were retrieved, and the DMEM was collected to assess the calcium and phosphorus ions using induced coupled plasma-optical emission spectroscopy (ICP-OES, iCAP 6300 duo plasma emission spectrometer).[45] Each point of time was analyzed in triplicate. Ca and P precipitation from DMEM after incubation with CaP-CHI-HA and CaP was reported based on the percent remaining in solution relative to that of the DMEM-only controls using the following equation:

$$\%\ \text{Ca or P remaining in DMEM solution} = \frac{[x]}{[\text{DMEM}]} \times 100$$

where $[x]$ is the ion concentration in the solution and [DMEM] is the ion concentration of the DMEM with the coverslip.

4. Substrate Characterization. *4.1. Scanning Electron Microscopy.* SEM investigations were performed with an LaB6 electron microscope (JEOL JSM-5400LV) on sputter-coated CaP-CHI-HA and CaP coatings with thin gold−palladium film (JEOL ion sputter JFC 1100). Images were acquired from secondary electrons at a primary beam energy of 10 kV.

4.2. Transmission Electron Microscopy. TEM investigations were performed with a JEOL ARM 200F cold FEG TEM/STEM (point resolution 0.19 nm in TEM mode and 0.078 nm in STEM mode) fitted with a GIF Quatum ER. HR-TEM pictures were performed with a JEOL ARM 200F cold FEG (point resolution 0.19 nm) fitted with a GIF Quatum ER.

4.3. Infrared Microspectroscopy. IR spectra were recorded between 4000 and 800 cm^{-1} on a Bruker Vertex 70v spectrometer equipped with a Hyperion 2000 microscope and a 15× objective. A KBr beam splitter and an MCT detector were used. The resolution of the single beam spectra was 4 cm^{-1}. Spectra of CaF_2 substrates coated with CaP-CHI-HA or CaP were recorded in transmission mode. Masks of 100 × 100 μm or 85 × 85 μm were used to record the maps. The number of bidirectional double-sided interferogram scans was 32, which corresponds to a 20 s accumulation. All interferograms were Fourier processed using the Mertz phase correction mode and a Blackman-Harris three-term apodization function. Measurements were performed at 21 ± 1 °C in an air-conditioned room. Water vapor subtraction was performed when necessary.

4.4. Near Infrared Confocal Raman Microspectroscopy. Spectra were recorded between 1800 and 500 cm^{-1} with a spectral resolution of 4 cm^{-1} on a Labram ARAMIS instrument (Horiba Jobin Yvon S.A.S., France) with a 100× objective (Olympus, BX41, France). Data acquisition was carried out by means of the LabSpec 5 software (Horiba Jobin Yvon S.A.S. France). Masks of 100 × 100 μm were used to record the maps with 25 analyzed points. All spectra were then preprocessed using baseline removal (LB) with a polynomial of order four followed by standard normal variate (SNV) methods to remove physical phenomena such as the scatter (interferences) and the influence of noises.

4.5. Atomic Force Microscopy. AFM was performed in contact mode and both in air and aqueous medium in wet conditions (DMEM without phenol red) at room temperature using an AFM MFP3D-BIO instrument. The applied force between the tip and the surface was carefully monitored and minimized at about 0.25 nN, and all images were collected with a resolution of 512 × 512 pixels and a scan rate of 1 Hz. The nanoindentation method provides the Young's modulus calculated from the force versus indentation curve. Triangular cantilevers were purchased from Bruker (MLCT, Bruker-nano AXS). The spring constants of the cantilevers were calculated in the range of 12−16 pN/nm using the thermal noise method. Maps of mechanical properties (FVI for force volume image) were obtained by recording a grid map of 50 × 50 force curves at different 80 × 80 μm locations on the samples. The maximum loading force was 5 nN. Maps of mechanical and adhesive properties and the corresponding histograms (statistical distribution) were estimated from the analysis of the approach curves according to the Sneddon model;[46] within the framework of Sneddon theory, the loading force F depends on the indentation depth δ according to

$$F = \frac{2E\text{Tan}(\propto)}{\pi(1-\nu^2)}\delta^2 f_{\text{BECC}}$$

where δ is the indentation depth, ν is the Poisson coefficient, α is the semitop angle of the tip, and f_{BECC} is the bottom effect cone correction function that takes into account the stiffness of the film-supporting substrate.[47] FVI were performed at a 0.5 Hz scan rate and with maximal loading/pulling speed of about 2 μm/s. Then, they were analyzed by means of an automatic Matlab algorithm described elsewhere.[48] Briefly, the physicochemical parameters involved in the Sneddon model[40] were estimated from the raw data using a nonlinear regression procedure. The method used was based on advanced tools for "segmenting" the force curves, i.e., automatically detecting the tip-to-surface contact point with accuracy.

5. Wharton's Jelly Stem Cells. Human umbilical cord harvesting was approved ethically and methodologically by our local Research Institution and was conducted with informed patients (written consent) in accordance with the usual ethical legal regulations (Article R 1243-57). All procedures were done in accordance with our authorization and registration number DC-2014-2262 given by the

DOI: 10.1021/acsami.7b01665
ACS Appl. Mater. Interfaces 2017, 9, 12791−12801

National "Cellule de Bioéthique". WJ-SCs were enzymatically isolated from fresh human umbilical cords obtained after full-term births (according to Mechiche Alami et al.[30]). WJ-SCs were amplified at density of 3×10^3 cell/cm^2 in α-MEM culture medium supplemented with 10% decomplemented FBS, 1% penicillin/streptomycin/amphotericin B and 1% glutamax (v/v, Gibco) and maintained in a humidified atmosphere of 5% CO_2 at 37 °C with a medium change every 2 days. At third passage, WJ-SCs were characterized by flow cytometry (FACSCalibur; BD Bioscience) through the expression of CD73, CD90, CD44, CD105, CD34, CD45, and HLA-DR and then used in our experimental procedure at the fourth passage. WJ-SCs were seeded in 24 well plates at 24 000 cells/cm^2 on UV-decontaminated CaP-CHI-HA. UV-decontaminated CaP and coverslips were used as controls.

5.1. Cytoskeleton Vinculin Staining. After 5 days of culture on CaP-CHI-HA and controls, WJ-SCs were fixed in 4% (w/v) paraformaldehyde (Sigma-Aldrich) at 37 °C for 10 min. Cells were then permeabilized with 0.5% (v/v) Triton X-100 for 15 min and blocked in 3% (v/v) bovine serum albumin (BSA) (Sigma-Aldrich) in DPBS for 1 h at room temperature. After being blocked, cells were incubated overnight with a mouse polyclonal antibody targeting vinculin (US-Biological) at a 1/25 dilution in blocking buffer. After two rinses with DPBS, a secondary antimouse biotinylated antibody (Invitrogen) was used at a 1/50 dilution for 30 min at room temperature followed by Alexa 594-conjugated streptavidin at 1/200 dilution (Invitrogen) for 30 min at room temperature. Alexa 488-phalloidin (1/100 dilution in 0.1% Triton X-100) was used to stain F-actin for 45 min at room temperature. Nuclei were counter-stained with 4,6-diamidino-2-phenylindole (DAPI, 100 ng/mL, 1/10 000 dilution) for 5 min. Stained cells were mounted and imaged by laser scanning (Zeiss LSM 710 NLO, 63× oil immersion objective, Numerical Aperture 1.4, Germany). Image analysis and 3D visualization were performed using ImageJ and Imaris softwares (Bitplane, Switzerland), respectively.

5.2. Chromatin Condensation. Chromatin condensation parameter (CCP) was determined using homemade ImageJ macro based on protocol defined in ref 49. The first step of the macro was an image segmentation to transform fluorescence images of the nucleus in binary images. Then, a skeletonized algorithm using Sobel edge detection filters was applied to detect chromatin. The nucleus outline was determined and removed from the skeleton image. The CCP parameter was then determined by calculating the area percentage of detected pixels on the nucleus surface.

5.3. Integrin α2 and β1, Runx-2, Osteopontin, and Osteocalcin Immunolabeling. After five days of culture on CaP-CHI-HA and on controls, fixed and permeabilized WJ-SCs were prepared as previously. After being blocked, cells were incubated overnight with mouse monoclonal antibodies targeting α2 or β1 integrin subunits, Runx-2 (at a 1/100 dilution in blocking buffer, Santa Cruz Biotechnology), and with rabbit polyclonal antibodies targeting osteopontin and osteoclacin (at a 1/100 dilution in blocking buffer, Calbiochem). After the cells were rinsed twice with DPBS, secondary horse antimouse and goat antirabbit IgG biotinylated antibodies (Invitrogen) were used at a 1/100 dilution for 30 min at room temperature followed by Alexa 488-conjugated streptavidin at 1/200 dilution (Invitrogen) for 30 min at room temperature. Nuclei were counter-stained with DAPI. The stained cells were mounted and imaged by laser scanning microscopy (Zeiss LSM 710 NLO, 20× objective, numerical aperture 0.8 for integrins and 63× oil immersion objective, numerical aperture for Runx-2, OPN, and OCN).

5.4. Wharton's Jelly Stem Cell Stiffness. After 5 days of culture on CaP-CHI-HA and controls, WJ-SCs were fixed in 1% (w/v) paraformaldehyde at 37 °C for 10 min. Cell topography and cell stiffness were followed by AFM (MFP3D-BIO instrument) as previously described.

5.5. ELISA. After 5 days of culture on CaP-CHI-HA and controls, supernatants were collected and stored at −20 °C, and samples were subsequently assessed in duplicate for specific cytokine. Secreted levels of OPG, VEGF, and BMP-2 were assessed using Duoset human osteoprotegerin/TNFRSF11B, Duoset human VEGF, and Duoset human BMP-2 (R&D systems), respectively, according to the manufacturer's instructions. Optical densities were measured at 450 nm using a microplate reader (FLUOstar Omega microplate reader, BMG Labtech); the released amount of cytokines was calculated from the corresponding standard curves and normalized to total protein content (measured using the Nanodrop protein assay setup, Nanodrop, Thermo Scientific).

6. Bacteria Assay. The strain studied is a wild-type strain of *S. aureus* from Institut Pasteur Collection (CIP 53.154). After a preculture for 18 h in nutritive broth, 500 μL of minimal medium (MM composed of 62 mM potassium phosphate buffer, pH 7.0, 7 mM $[(NH_4)_2SO_4$, 2 mM $MgSO_4$, 10 μM $FeSO_4]$ with 0.4% (w/v) glucose) containing about 10^6 CFU/mL, controlled by enumeration, were deposited on CaP-CHI-HA and CaP, entirely covering them, for 48 h at 37 °C. Both coatings were rinsed with MM, immersed in 2 mL of MM, and sonicated for 5 min. Then, serial dilutions were plated, and colony counts were performed to evaluate adhesive activity. At least three independent enumerations were carried out for each surface, and all types of surfaces were tested six times.

7. Statistical Analysis. All statistical analyses were performed using GraphPad Prism 5 software. ICP-OES measurements were performed in triplicate with three replicates per sample. Data are presented as mean ± SD (pairwise comparisons were performed using unpaired *t*-test). All biological experiments were performed with six independent umbilical cords. ELISA and bacterial histograms represents mean ± SEM (Mann & Withney). AFM, nuclear volume, and CCP results are presented as media (Mann & Withney). For each test, a value of $p < 0.05$ was accepted as statistically significant p (rejection level of the null-hypothesis of equal means).

■ ASSOCIATED CONTENT

Supporting Information

The Supporting Information is available free of charge on the ACS Publications website at DOI: 10.1021/acsami.7b01665.

Details of chemical characterization by Raman and infrared microspectroscopies, high resolution transmission electron microscopy, and stem cell imaging by confocal laser scanning microscopy and 3D Imaris reconstruction (PDF)

■ AUTHOR INFORMATION

Corresponding Author

*E-mail: halima.kerdjoudj@univ-reims.fr.

ORCID

F. Boulmedais: 0000-0002-4934-9276

H. Kerdjoudj: 0000-0002-8072-9728

Author Contributions

●H.R. and M.D. contributed equally to this work.

Notes

The authors declare no competing financial interest.

■ ACKNOWLEDGMENTS

The authors are very grateful to the staff of Reims Maternity Hospital for providing umbilical cords and the staff of the Core PICT (URCA). This work was partially supported by IMACELL from CNRS project. M.D. is supported by a doctoral fellowship from the High Education French Minister. We thank Dr. J. Hemmerlé from INSERM U1121 (Université de Strasbourg, France) for SSCI setup, Dr. F. Velard for technical help, Dr. A. Beljebbar for Raman spectroscopy analysis, and Dr. S. Mechiche-Alami and Dr. S. Sayen for ICP experiments.

DOI: 10.1021/acsami.7b01665
ACS Appl. Mater. Interfaces 2017, 9, 12791−12801

REFERENCES

(1) Wang, P.; Zhao, L.; Liu, J.; Weir, M. D.; Zhou, X.; Xu, H. H. K. Bone Tissue Engineering via Nanostructured Calcium Phosphate Biomaterials and Stem Cells. *Bone Res.* **2014**, *2*, 14017.

(2) Collins, M. N.; Birkinshaw, C. Hyaluronic Acid Based Scaffolds for Tissue Engineering—A review. *Carbohydr. Polym.* **2013**, *92*, 1262−1279.

(3) Kim, I. Y.; Seo, S. J.; Moon, H. S.; Yoo, M. K.; Park, I. Y.; Kim, B. C.; Cho, C. S. Chitosan and its Derivatives for Tissue Engineering Applications. *Biotechnol. Adv.* **2008**, *26*, 1−21.

(4) Gentile, P.; Carmagnola, I.; Nardo, T.; Chiono, V. Layer-by-Layer Assembly for Biomedical Applications in the Last Decade. *Nanotechnology* **2015**, *26*, 422001.

(5) Wang, Z.; Wu, G.; Feng, Z.; Bai, S.; Dong, Y.; Wu, G.; Zhao, Y. Microarc-Oxidized Titanium Surfaces Functionalized with MicroRNA-21-Loaded Chitosan/Hyaluronic Acid Nanoparticles Promote the Osteogenic Differentiation of Human Bone Marrow Mesenchymal Stem Cells. *Int. J. Nanomed.* **2015**, *10*, 6675−6687.

(6) Tan, H.; Chu, C. R.; Payne, K. A.; Marra, K. G. Injectable in Situ Forming Biodegradable Chitosan-Hyaluronic Acid Based Hydrogels for Cartilage Tissue Engineering. *Biomaterials* **2009**, *30*, 2499−24506.

(7) Miranda, D. G.; Malmonge, S. M.; Campos, D. M.; Attik, N. G.; Grosgogeat, B.; Gritsch, K. A Chitosan-Hyaluronic Acid Hydrogel Scaffold for Periodontal Tissue Engineering. *J. Biomed. Mater. Res., Part B* **2016**, *104*, 1691−1702.

(8) Verma, D.; Katti, K. S.; Katti, D. R. Effect of Biopolymers on Structure of Hydroxyapatite and Interfacial Interactions in Biomimetically Synthesized Hydroxyapatite/Biopolymer Nanocomposites. *Ann. Biomed. Eng.* **2008**, *36*, 1024−1032.

(9) Popa, G.; Boulmedais, F.; Zhao, P.; Hemmerlé, J.; Vidal, L.; Mathieu, E.; Félix, O.; Schaaf, P.; Decher, G.; Voegel, J. C. Nanoscale Precipitation Coating: the Deposition of Inorganic Films Through Step-by-Step Spray-Assembly. *ACS Nano* **2010**, *4*, 4792−4798.

(10) Mechiche Alami, S.; Rammal, H.; Boulagnon-Rombi, C.; Velard, F.; Lazar, F.; Drevet, R.; Laurent Maquin, D.; Gangloff, S. C.; Hemmerlé, J.; Voegel, J. C.; Francius, G.; Schaaf, P.; Boulmedais, F.; Kerdjoudj, H. Harnessing Wharton's Jelly Stem Cell Differentiation into Bone-like Nodule on Calcium Phosphate Substrate Without Osteoinductive Factors. *Acta Biomater.* **2017**, *49*, 575−589.

(11) Khor, E.; Lim, L. Y. Implantable Applications of Chitin and Chitosan. *Biomaterials* **2003**, *24*, 2339−2349.

(12) Wang, X.; Xu, S.; Zhou, S.; Xu, W.; Leary, M.; Choong, P.; Qian, M.; Brandt, M.; Xie, Y. M. Topological Design and Additive Manufacturing of Porous Metals for Bone Scaffolds and Orthopaedic Implants: A Review. *Biomaterials* **2016**, *83*, 127−141.

(13) Leon, B.; Jansen, J. A. *Thin Calcium Phosphate Coatings for Medical Implants*; Springer: New York, 2009.

(14) Zeiger, D. N.; Miles, W. C.; Eidelman, N.; Lin-Gibson, S. Cooperative Calcium Phosphate Nucleation within Collagen Fibrils. *Langmuir* **2011**, *27*, 8263−8268.

(15) Xu, J.; Butler, I. S.; Gilson, D. F. R. FT-Raman and High-pressure Infrared Spectroscopic Studies of Dicalcium Phosphate Dihydrate ($CaHPO_4{\cdot}2H_2O$) and Anhydrous Dicalcium Phosphate ($CaHPO_4$). *Spectrochim. Acta, Part A* **1999**, *55*, 2801−2809.

(16) Pleshko, N.; Boskey, A.; Mendelsohn, R. Novel Infrared Spectroscopic Method for the Determination of Crystallinity of Hydroxyapatite Minerals. *Biophys. J.* **1991**, *60*, 786−793.

(17) Lei, Y.; Xu, Z.; Ke, Q.; Yin, W.; Chen, Y.; Zhang, C.; Guo, Y. Strontium Hydroxyapatite/Chitosan Nanohybrid Scaffolds with Enhanced Osteoinductivity for Bone Tissue Engineering. *Mater. Sci. Eng., C* **2017**, *72*, 134−142.

(18) Place, E. S.; Evans, N. D.; Stevens, M. M. Complexity in Biomaterials for Tissue Engineering. *Nat. Mater.* **2009**, *8*, 457−470.

(19) Hoppe, A.; Güldal, N. S.; Boccaccini, A. R. A Review of the Biological Response to Ionic Dissolution Products from Bioactive Glasses and Glass-Ceramics. *Biomaterials* **2011**, *32*, 2757−2774.

(20) Šupová, M. Problem of Hydroxyapatite Dispersion in Polymer Matrices: a Review. *J. Mater. Sci.: Mater. Med.* **2009**, *20*, 1201−1213.

(21) Chen, J.; Yu, Q.; Zhang, G.; Yang, S.; Wu, J.; Zhang, Q. Preparation and Biocompatibility of Nanohybrid Scaffolds by In Situ Homogeneous Formation of Nano Hydroxyapatite from Biopolymer Polyelectrolyte Complex for Bone Repair Applications. *Colloids Surf., B* **2012**, *93*, 100−107.

(22) Yamaguchi, I.; Tokuchi, K.; Fukuzaki, H.; Koyama, Y.; Takakuda, K.; Monma, H.; Tanaka, J. Preparation and Microstructure Analysis of Chitosan/Hydroxyapatite Nanocomposites. *J. Biomed. Mater. Res.* **2001**, *55*, 20−27.

(23) Wang, Y.; Chen, X.; Cao, W.; Shi, Y. Plasticity of Mesenchymal Stem Cells in Immunomodulation: Pathological and Therapeutic Implications. *Nat. Immunol.* **2014**, *15*, 1009−1016.

(24) Mastri, M.; Lin, H.; Lee, T. Enhancing the Efficacy of Mesenchymal Stem Cell Therapy. *World J. Stem Cells* **2014**, *6*, 82−93.

(25) Mechiche Alami, S.; Gangloff, S. C.; Laurent-Maquin, D.; Wang, Y.; Kerdjoudj, H. Concise Review: In Vitro Formation of Bone-Like Nodules Sheds Light on the Application of Stem Cells for Bone Regeneration. *Stem Cells Transl. Med.* **2016**, *5*, 1587−1593.

(26) McMurray, R. J.; Dalby, M. J.; Tsimbouri, P. M. Using Biomaterials to Study Stem Cell Mechanotransduction, Growth and Differentiation. *J. Tissue Eng. Regener. Med.* **2015**, *9*, 528−539.

(27) Grashoff, C.; Hoffman, B. D.; Brenner, M. D.; Zhou, R.; Parsons, M.; Yang, M. T.; McLean, M. A.; Sligar, S. G.; Chen, S. C.; Ha, T.; Schwartz, M. A. Measuring Mechanical Tension Across Vinculin Reveals Regulation of Focal Adhesion Dynamics. *Nature* **2010**, *466*, 263−266.

(28) Yim, E. K. F.; Darling, E. M.; Kulangara, K.; Guilak, F.; Leong, K. W. Nanotopography-Induced Changes in Focal Adhesions, Cytoskeletal Organization, and Mechanical Properties of Human Mesenchymal Stem Cells. *Biomaterials* **2010**, *31*, 1299−1306.

(29) Maytin, E. V. Hyaluronan: More than Just a Wrinkle Filler. *Glycobiology* **2016**, *26*, 553−559.

(30) Mechiche Alami, S.; Velard, F.; Draux, F.; Siu Paredes, F.; Josse, J.; Lemaire, F.; Gangloff, S. C.; Graesslin, O.; Laurent Maquin, D.; Kerdjoudj, H. Gene Screening of Wharton's Jelly Derived Stem Cells. *Biomed. Mater. Eng.* **2014**, *24*, 53−61.

(31) Dalby, M. J.; Gadegaard, N.; Oreffo, R. O. C. Harnessing Nanotopography and Integrin-Matrix Interactions to Influence Stem Cell Fate. *Nat. Mater.* **2014**, *13*, 558−569.

(32) Pajerowski, J. D.; Dahl, K. N.; Zhong, F. L.; Sammak, P. J.; Discher, D. E. Physical Plasticity of the Nucleus in Stem Cell Differentiation. *Proc. Natl. Acad. Sci. U. S. A.* **2007**, *104*, 15619−15624.

(33) Efroni, S.; Duttagupta, R.; Cheng, J.; Dehghani, H.; Hoeppner, D. J.; Dash, C.; Bazett-Jones, D. P.; Le Grice, S.; McKay, R. D. G.; Buetow, K. H.; Gingeras, T. R.; Misteli, T.; Meshorer, E. Global Transcription in Pluripotent Embryonic Stem Cells. *Cell Stem Cell.* **2008**, *2*, 437−447.

(34) Heo, S. J.; Thorpe, S. D.; Driscoll, T. P.; Duncan, R. L.; Lee, D. A.; Mauck, R. L. Biophysical Regulation of Chromatin Architecture Instills a Mechanical Memory in Mesenchymal Stem Cells. *Sci. Rep.* **2015**, *5*, 16895.

(35) Eckfeldt, C. E.; Mendenhall, E. M.; Verfaillie, C. M. The Molecular Repertoire of the 'Almighty' Stem Cell. *Nat. Rev. Mol. Cell Biol.* **2005**, *6*, 726−737.

(36) Müller, C.; Leutz, A. Chromatin Remodeling in Development and Differentiation. *Curr. Opin. Genet. Dev.* **2001**, *11*, 167−174.

(37) Olivares-Navarrete, R.; Hyzy, S. L.; Hutton, D. L.; Erdman, C. P.; Wieland, M.; Boyan, B. D.; Schwartz, Z. Direct and Indirect Effects of Microstructured Titanium Substrates on the Induction of Mesenchymal Stem Cell Differentiation Towards the Osteoblast Lineage. *Biomaterials* **2010**, *31*, 2728−2735.

(38) Sharaf-Eldin, W. E.; Abu-Shahba, N.; Mahmoud, M.; El-Badri, N. The Modulatory Effects of Mesenchymal Stem Cells on Osteoclastogenesis. *Stem Cells Int.* **2016**, *2016*, 1−13.

(39) Proksch, S.; Bittermann, G.; Vach, K.; Nitschke, R.; Tomakidi, P.; Hellwig, E. hMSC-Derived VEGF Release Triggers the Chemoattraction of Alveolar Osteoblasts. *Stem Cells* **2015**, *33*, 3114−3124.

(40) James, A. W.; LaChaud, G.; Shen, J.; Asatrian, G.; Nguyen, V.; Zhang, X.; Ting, K.; Soo, C. A Review of the Clinical Side Effects of

DOI: 10.1021/acsami.7b01665
ACS Appl. Mater. Interfaces 2017, 9, 12791−12801

Bone Morphogenetic Protein-2. *Tissue Eng., Part B* **2016**, *22*, 284−297.
(41) Josse, J.; Velard, F.; Gangloff, S. C. Staphylococcus aureus vs. Osteoblast: Relationship and Consequences in Osteomyelitis. *Front. Cell. Infect. Microbiol.* **2015**, *5*, 85.
(42) Chua, P. H.; Neoh, K. G.; Shi, Z.; Kang, E. T. Structural Stability and Bioapplicability Assessment of Hyaluronic Acid−Chitosan Polyelectrolyte Multilayers on Titanium Substrates. *J. Biomed. Mater. Res., Part A* **2008**, *87A*, 1061−1074.
(43) Hernandez-Montelongo, J.; Lucchesi, E. G.; Gonzalez, I.; Macedo, W. A. A.; Nascimento, V. F.; Moraes, A. M.; Beppu, M. M.; Cotta, M. A. Hyaluronan/Chitosan Nanofilms Assembled Layer-by-Layer and Their Antibacterial Effect: A Study using Staphylococcus aureus and Pseudomonas aeruginosa. *Colloids Surf., B* **2016**, *141*, 499−506.
(44) Cado, G.; Kerdjoudj, H.; Chassepot, A.; Lefort, M.; Benmlih, K.; Hemmerlé, J.; Voegel, J. C.; Jierry, L.; Schaaf, P.; Frère, Y.; Boulmedais, F. Polysaccharide Films Built by Simultaneous or Alternate Spray: a Rapid Way to Engineer Biomaterial Surfaces. *Langmuir* **2012**, *28*, 8470−8478.
(45) Velard, F.; Schlaubitz, S.; Fricain, J. C.; Guillaume, C.; Laurent-Maquin, D.; Möller-Siegert, J.; Vidal, L.; Jallot, E.; Sayen, S.; Raissle, O.; Nedelec, J. M.; Vix-Guterl, C.; Anselme, K.; Amédée, J.; Laquerrière, P. In Vitro and In Vivo Evaluation of the Inflammatory Potential of Various Nanoporous Hydroxyapatite Biomaterials. *Nanomedicine* **2015**, *10*, 785−802.
(46) Sneddon, I. N. The Relation Between Load and Penetration in the Axisymmetric Boussinesq Problem for a Punch of Arbitrary Profile. *Int. J. Eng. Sci.* **1965**, *3*, 47−57.
(47) Gavara, N.; Chadwick, R. S. Determination of the Elastic Moduli of Thin Samples and Adherent Cells using Conical Atomic Force Microscope Tips. *Nat. Nanotechnol.* **2012**, *7*, 733−736.
(48) Polyakov, P.; Soussen, C.; Duan, J.; Duval, J. F. L.; Brie, D.; Francius, G. Automated Force Volume Image Processing for Biological Samples. *PLoS One* **2011**, *6*, e18887.
(49) Irianto, J.; Lee, D. A.; Knight, M. M. Quantification of Chromatin Condensation Level by Image Processing. *Med. Eng. Phys.* **2014**, *36*, 412−417.

DOI: 10.1021/acsami.7b01665
ACS Appl. Mater. Interfaces 2017, 9, 12791−12801